Uncovering the 3d and 4d Electronic Interactions in Solvated Ru Complexes with 2p3d Resonant Inelastic X-ray Scattering

Benjamin I. Poulter, Elisa Biasin, Stanisław H. Nowak, Thomas Kroll, Roberto Alonso-Mori, Robert W. Schoenlein, Niranjan Govind, Dimosthenis Sokaras,* and Munira Khalil*

ABSTRACT: The electronic structure and dynamics of ruthenium complexes are widely studied given their use in catalytic and light-harvesting materials. Here we investigate three model Ru complexes, $[Ru^{III}(NH_3)_6]^{3+}$, $[Ru^{II}(bpy)_3]^{2+}$, and $[Ru^{II}(CN)_6]^{4-}$, with L_3-edge 2p3d resonant inelastic X-ray scattering (RIXS) to probe unoccupied 4d valence orbitals and occupied 3d orbitals and to gain insight into the interactions between these levels. The 2p3d RIXS maps contain a higher level of spectral information than the L_3 X-ray absorption near edge structure (XANES). This study provides a direct measure of the 3d spin−orbit splittings of 4.3, 4.0, and 4.1 eV between the $3d_{5/2}$ and $3d_{3/2}$ orbitals of the $[Ru^{III}(NH_3)_6]^{3+}$, $[Ru^{II}(bpy)_3]^{2+}$, and $[Ru^{II}(CN)_6]^{4-}$ complexes, respectively.

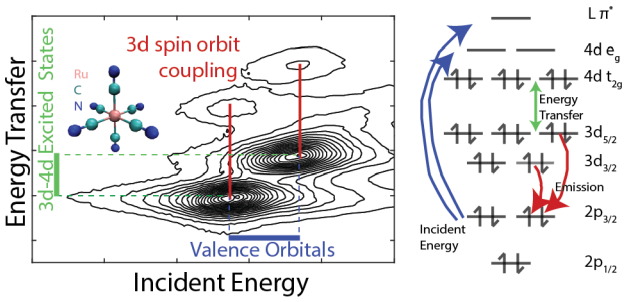

INTRODUCTION

Ruthenium complexes are extensively studied due to their unique photophysical, photochemical, and catalytic properties[1−3] and have found widespread use in light-harvesting technologies, catalysis, and biological applications.[4−6] The modulation of the ground and excited state valence electronic structure of Ru-complexes by varying their ligand environments determines their functionality and has been the focus of numerous experimental and computational studies.[1,7] For example, ruthenium(II) photosensitizers employ the long lifetimes of photoexcited low-lying metal-to-ligand charge transfer (MLCT) states, where a Ru 4d electron is transferred to a ligand π^* orbital, to enable efficient charge extraction.[8,9] In other applications, such as photocatalysis, the formation of excited metal-centered (MC) states governs excited state reactivity.[10] Despite significant experimental and theoretical efforts focused on understanding Ru complexes and their excited states in photochemical and catalytic environments, there exists a knowledge gap in developing a quantitative, molecular-level description of the electronic couplings of the 4d electrons, the complex continuum of excited states, and the metal−ligand interactions in Ru based complexes. Developing new experimental and theoretical tools to address this knowledge gap is vital for designing the next generation of 4d functional materials.

The development of the field of X-ray spectroscopy at third-generation synchrotron sources has resulted in ideal experimental tools with element and orbital specificity to understand the electronic structure of transition metal complexes in greater detail.[11,12] X-ray absorption spectroscopy (XAS) is most often used to probe unoccupied valence states and has been used at the K- (1s core hole) and L- (2p core hole) edges to gain significant insight into the 4d electronic configurations of Ru molecular systems as a function of coordination geometry, oxidation state, and ligand identity.[13,14] X-ray emission spectroscopy (XES) is a complementary technique to XAS as it reports on the occupied electronic states with element specificity.[15] These two techniques can be combined by monitoring the XES spectrum as a function of the incident energy tuned across the XANES (X-ray absorption near-edge structure) region and is known as resonant-inelastic X-ray scattering (RIXS). The RIXS spectra are often displayed as 2D maps plotted as incident energy vs energy transfer (the difference between the absorbed and emitted X-ray photons) and contain unique information about the local electronic structure of the complexes under investigation.[16]

Recent L-edge RIXS studies have shown it to be an extremely powerful technique for mapping transition metal electronic structure.[17,18] In particular, RIXS spectroscopy has identified metal-centered excited states[19,20] and illuminated their role in ultrafast photochemical processes.[20,21] However, L-edge RIXS has been primarily focused on first-row transition metal complexes with only a few examples of 4d[22−25] and

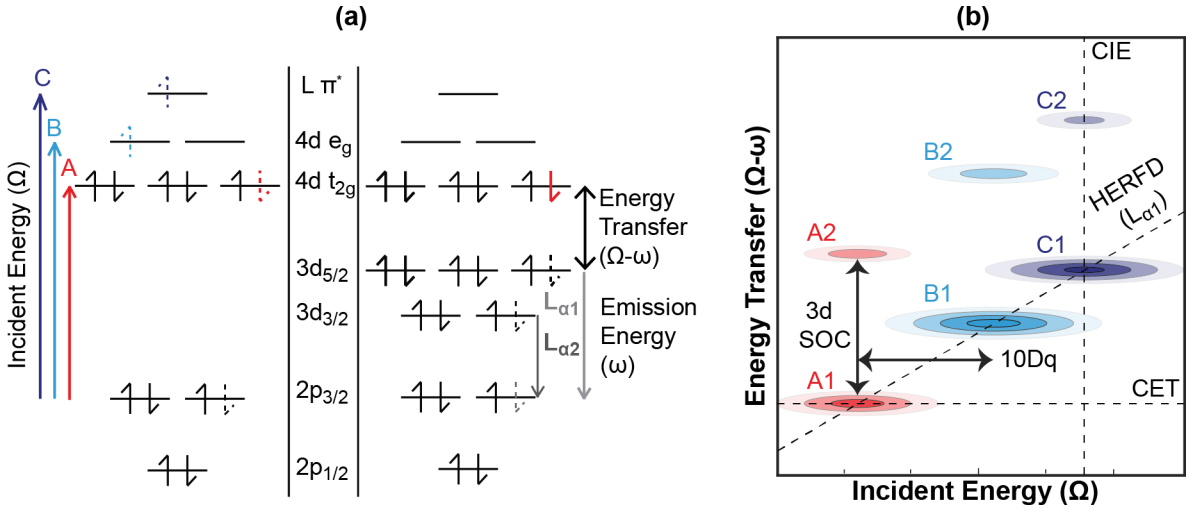

Figure 1. (a) Energy level diagram depicting the two-step Ru L_3-edge 2p3d RIXS process. Initially, a $2p_{3/2}$ electron is excited by an X-ray photon of incident energy (IE), Ω. Depending on the Ru system being investigated, three resonant transitions are possible involving excitation into either the t_{2g} (A), e_g (B), or ligand π^* (C) orbitals. After this excitation, a photon of energy ω (emission energy, EE) is emitted corresponding to the relaxation of either a $3d_{5/2}$ or $3d_{3/2}$ electron to fill the $2p_{3/2}$ hole. The energy difference between IE and EE, $\Omega - \omega$ (energy transfer, ET), corresponds to the 3d-4d splitting and can give insight into potential 3d-4d couplings. (b) Cartoon Ru 2p3d RIXS map presented in ET vs IE. Three sets of features are present: A, B, and C which correspond to those seen in the diagram. Along a diagonal cut (constant emission energy), lie either the A1, B1, and C1 features ($L\alpha_1$ emission) or the A2, B2, and C2 features ($L\alpha_2$ emission). The constant emission energy cut at the peak of the $L\alpha_1$ energy is referred to as the high energy resolution fluorescence detection (HERFD) L_3-edge XANES spectrum. The energy splitting between the 1 and 2 peaks in a given feature, i.e., A2−A1, corresponds to the 3d spin−orbit coupling. Taking cuts at a constant energy transfer (CET) reports on states with the same final state configuration but different intermediate states. Conversely, cuts at a constant incident energy report on states with the same intermediate state configuration but different final states. The resolution in either direction depends on the lifetime of the intermediate (IE axis) or the final (ET axis) state. The separation between different features, i.e., B−A, report on splittings in the valence electronic structure such as the e_g - t_{2g} or 10 Dq energy.

5d[26,27] solid state systems. In this work, we use the Ru L_3 2p3d RIXS, illustrated in Figure 1(a), to investigate a selection of model Ru complexes: $[Ru^{III}(NH_3)_6]^{3+}$, a Ru^{III} complex with primarily σ donating ligands; $[Ru^{II}(bpy)_3]^{2+}$, a photochemically relevant Ru^{II} complex with weak π accepting ligands; and $[Ru^{II}(CN)_6]^{4-}$, a Ru^{II} complex with significant metal−ligand π backbonding interactions. This study demonstrates that Ru 2p3d RIXS experiments measure the spin−orbit coupling of Ru 3d orbitals and that the positions and lineshapes of the 2p3d RIXS spectral features are extremely sensitive to 3d4d electronic correlations. Additionally, the Ru 2p3d RIXS experiment provides finer spectral resolution than a Ru L-edge XAS measurement as the lifetime broadening contribution from the 3d hole (RIXS final state) is less than that from the 2p hole (RIXS intermediate state) (~0.25 and ~2 eV, respectively).[28] The experimental spectra presented here will serve as benchmarks for the development of advanced theoretical tools to accurately calculate the electronic structure of Ru(II) and Ru(III) complexes and for interpreting the Ru 2p3d RIXS spectra of more complex systems in their electronic ground and photoexcited states.

METHODS

Samples. The complexes tris(2,2′-bipyridyl)ruthenium(II) chloride hexahydrate $[Ru^{II}(bpy)_3]Cl_2 \cdot 6(H_2O)$, potassium hexacyanoruthate(II) hydrate $K_4[Ru^{II}(CN)_6] \cdot x(H_2O)$, and hexammineruthenium(III) chloride $[Ru^{III}(NH_3)_6]Cl_3$ were purchased from Sigma-Aldrich and used without further purification. These complexes were dissolved in water to form aqueous solutions of 60 mM $[Ru^{II}(bpy)_3]^{2+}$, 100 mM $[Ru^{II}(CN)_6]^{4-}$, and 100 mM $[Ru^{III}(NH_3)_6]^{3+}$.

Data Acquisition and Analysis. The high-resolution X-ray absorption and emission spectroscopy experiments were performed at beamline 6−2a at the Stanford Synchrotron Radiation Lightsource (SSRL). A liquid nitrogen cooled Si(111) monochromator delivered an incident beam flux of 3×10^{12} photons/s at 3.0 keV (near the Ru L_3 absorption edge of 2.838 keV) with an energy resolution of ~0.4 eV and a beamsize with a full width half-maximum (fwhm) of 400 × 250 μm^2 ($v \times h$). The emitted X-rays were collected with a high-resolution Johansson-type spectrometer equipped with a cylindrically bent Si(111) analyzer with an energy resolution of ~0.32 eV at 2.4 keV.[29] The calibration of the spectrometer was performed with elastic scattering measurements.

An in-vacuum 2-dimensional (2048 pixels × 2048 pixels) charge coupled device (CCD) camera was used as a position-sensitive detector to record the dispersed X-rays. Each CCD image was corrected for background and geometrical effects before being projected along the energy dispersion axis to yield an emission spectrum. Pixel clustering and low-intensity thresholding were also applied to isolate X-ray events from electronic noise. The detailed procedure used for image processing is described elsewhere.[29] To construct the resonant inelastic X-ray scattering maps, the X-ray emission spectra were stacked according to the corresponding incident X-ray energies. These incident energy vs emission energy maps (SI Figure 2) were then converted to the incident energy vs energy transfer maps presented in this publication.

While the main volume of the spectrometer was under vacuum conditions in order to minimize the attenuation of these low-energy X-rays, the sample subchamber was filled with an ambient He atmosphere which allowed for the integration of a free-flowing liquid jet system. An HPLC pump was used to flow (7 mL/min flow rate) the samples through a 250 μm (inner diameter) Kapton capillary. A catcher placed 10 mm below the capillary was used to refeed the pump and enabled closed-loop recirculation of the solution. The X-ray beam interaction point was set ~2 mm below the tip of the Kapton capillary, and a downstream ionization chamber was used for the quick alignment of the jet and the incident beam.

RESULTS

Overview of Peak Positions and Assignments in Ru 2p3d RIXS Spectra. The Ru L_3 2p3d RIXS maps of $[Ru^{III}(NH_3)_6]^{3+}$, $[Ru^{II}(bpy)_3]^{2+}$, and $[Ru^{II}(CN)_6]^{4-}$, are shown in Figures 3, 4, and 5, respectively. Projecting the 2D RIXS spectra along the energy transfer axis, results in the partial fluorescence yield (PFY) XAS measurements shown in Figure 2 as solid lines. These spectra show three distinct pre-edge features labeled A, B, and C, and assigned previously[30,7] The A feature (~2838 eV) is due to a transition from the $2p_{3/2}$ orbitals to the vacancy in the Ru 4d t_{2g} orbitals and is present only for Ru(III) complexes. The B feature present in all measured Ru L_3-edge spectra (~2840.5 eV) is mainly due to transitions from the $2p_{3/2}$ orbitals to the unoccupied 4d e_g orbitals. Finally, the $[Ru^{II}(CN)_6]^{4-}$ spectrum displays a clear C feature (~2844 eV) which is due to transitions from the $2p_{3/2}$ orbitals to unoccupied ligand π^* orbitals. The same figures display the HERFD spectra (see Figure 1(b)) with reduced line widths due to the longer lifetime of a $3d_{5/2}$ core hole compared to that of a $2p_{3/2}$ core hole. The PFY spectra are fully broadened by the $2p_{3/2}$ core-hole lifetime. Due to this core-hole lifetime broadening suppression in the HERFD measurement, higher resolution peak splittings can be obtained and additional features may be seen such as the shoulder on the blue edge of the $[Ru^{III}(NH_3)_6]^{3+}$ B peak at ~2842 eV.

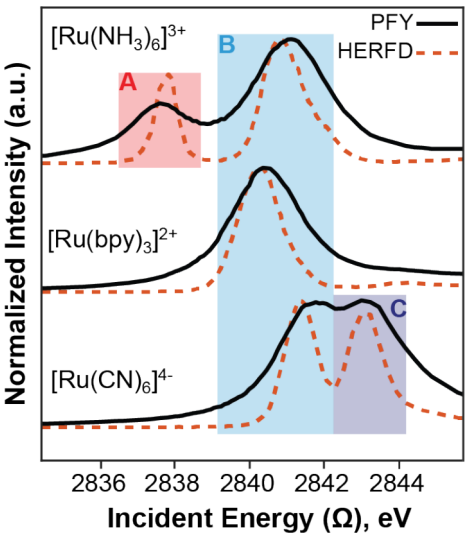

Figure 2. Ru L_3-edge XANES spectra for the model complexes $[Ru^{III}(NH_3)_6]^{3+}$, $[Ru^{II}(bpy)_3]^{2+}$, and $[Ru^{II}(CN)_6]^{4-}$. Partial fluorescence yield (PFY) and high energy resolution fluorescence detected (HERFD) spectra are shown. All complexes present B features ($2p_{3/2} \rightarrow e_g$). The spectra of $[Ru^{III}(NH_3)_6]^{3+}$ present an A feature ($2p_{3/2} \rightarrow t_{2g}$) as it is the only d^5 complex and thus has a hole in the t_{2g}. The $[Ru^{II}(CN)_6]^{4-}$ spectra show the presence of a C feature ($2p_{3/2} \rightarrow$ ligand π^*) due to strong metal–ligand interactions through π backbonding.

The 2p3d RIXS measurement allows for the features in the PFY spectra to be deconvoluted into numerous subpeaks along the energy transfer dimension providing insight into the electronic structure of Ru complexes in solution. In the case of $[Ru^{III}(NH_3)_6]^{3+}$, the A feature includes the A1 and A2 peaks, and the B feature is comprised of the B0, B1, and B2 peaks as shown in Figure 3(a). The map of the $[Ru^{II}(bpy)_3]^{2+}$ in Figure 4(a) presents an intense B feature which includes the B1 and B2 peaks. A weak C feature (C1 peak), nearly indistinguishable in the 1D spectrum, is also seen at higher energies. Finally, the $[Ru^{II}(CN)_6]^{4-}$ 2p3d RIXS map (Figure 5(a)) contains both a B feature with B1 and B2 peaks and a C feature with C1 and C2 peaks. The subpeaks 1 and 2 in a given feature (A, B, or C) occur at the same incident energies, are separated along the energy transfer axis, and involve $3d_{5/2}$ or $3d_{3/2}$ orbitals, respectively. The energy difference between these features corresponds to a direct observation of splitting due to 3d spin–orbit coupling (see Figure 1).

We further examine the 2D RIXS maps of the Ru complexes by looking at constant energy transfer cuts (CET, horizontal slices) and constant incident energy cuts (CIE, vertical slices) in Figures 3–5. Peaks lying along the same CET axis share the same final state in the RIXS process, and peaks along the same CIE axis, share the same intermediate state. One must be cautious when making these assignments, however, as energy splittings between individual states are often smaller than the

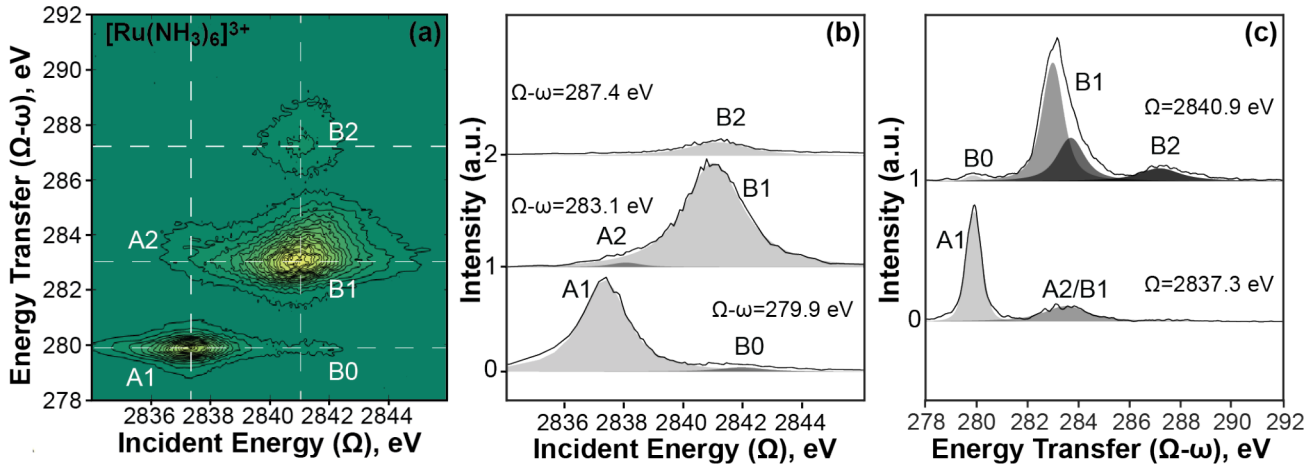

Figure 3. (a) Ru L_3-edge 2p3d RIXS map of $[Ru^{III}(NH_3)_6]^{3+}$. The following peaks are observed: A1 (2837.3 and 279.9 eV), A2 (2837.3 and 283.6 eV), B0 (2841.9 and 279.8 eV), B1 (2840.9 and 283.1 eV), and B2 (2840.9 and 287.4 eV). The white dashed lines correspond to the CET and CIE cuts pictured in (b) and (c), respectively. The map is normalized to the maximum of the B1 peak and drawn with 20 evenly spaced contour levels. b) CET cuts taken through the maxima of the A1 (0), B1 (1), and B2 (2) peaks. (c) CIE cuts taken through the maxima of the A1 (0) and B1 (1) peaks. The shaded regions in (b) and (c) are the Voigt profiles that result from fitting the spectra; fit parameters can be found in SI Figure 3.

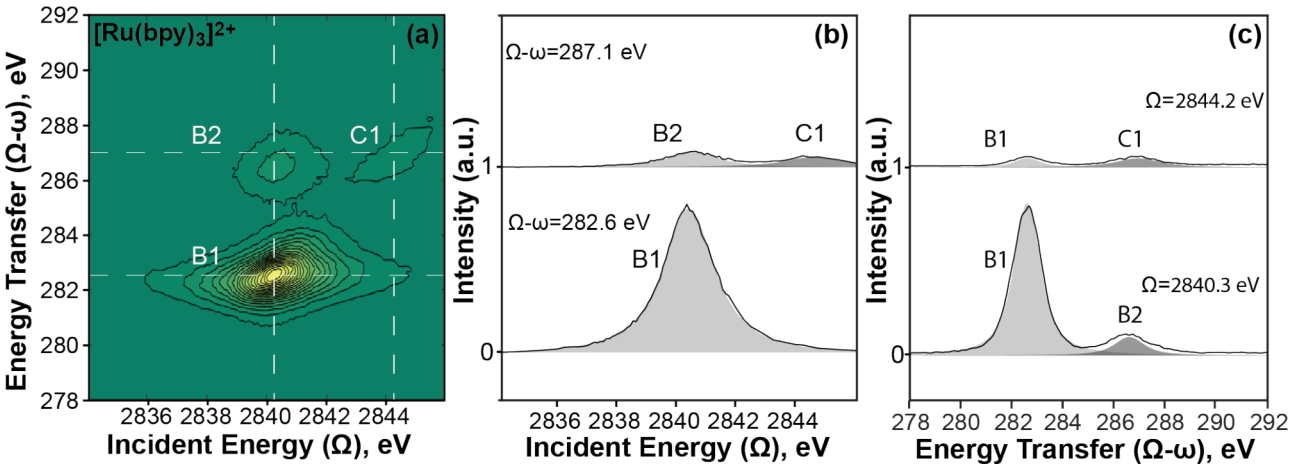

Figure 4. (a) Ru L_3-edge 2p3d RIXS map of $[Ru^{II}(bpy)_3]^{2+}$. The following peaks are observed: B1 (2840.3 and 282.6 eV), B2 (2840.3 and 286.6 eV), and C1 (2844.2 and 287.1 eV). The white dashed lines correspond to the CET and CIE cuts pictured in (b) and (c), respectively. The map is normalized to the maximum of the B1 peak and drawn with 20 evenly spaced contour levels. (b) CET cuts taken through the maxima of B1 (0) and C1 (1) peaks. (c) CIE cuts taken through the maxima of the B1 (0) and C1 (1) peaks. The shaded regions in (b) and (c) are the Voigt profiles that result from fitting the spectra; fit parameters can be found in SI Figure 4.

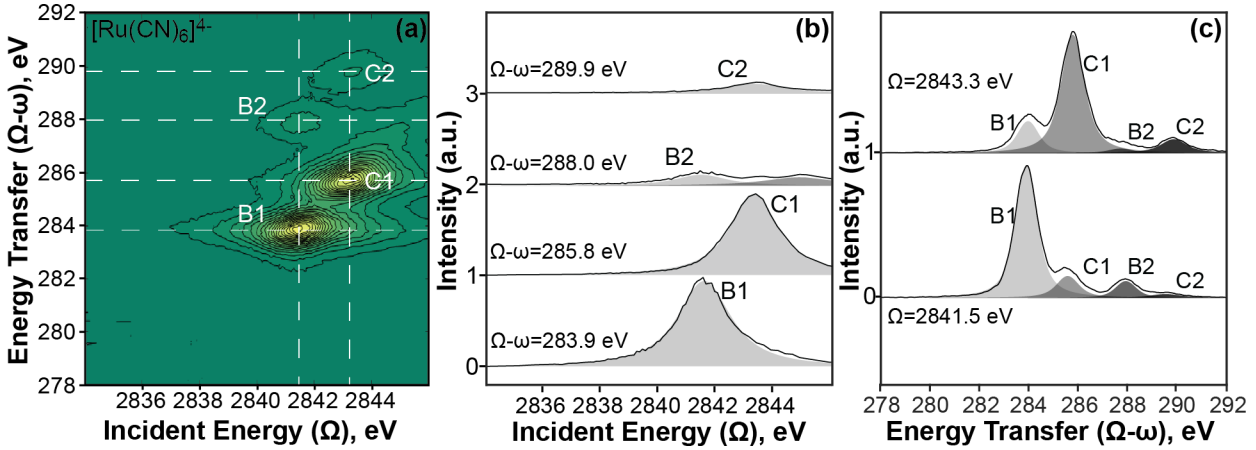

Figure 5. (a) Ru L_3-edge 2p3d RIXS map of $[Ru^{II}(CN)_6]^{4-}$. The following peaks are observed: B1 (2841.5 and 283.9 eV), B2 (2841.5 and 288.0 eV), C1 (2843.3 and 285.8 eV), and C2 (2843.3 and 289.9 eV). The white dashed lines correspond to the CET and CIE cuts pictured in (b) and (c), respectively. The map is normalized to the maximum of the B1 peak and drawn with 20 evenly spaced contour levels. (b) CET cuts taken through the maxima of B1 (0), C1 (1), B2 (2), and C2 (3) peaks. (c) CIE cuts taken through the maxima of the B1 (0) and C1 (1) peaks. The shaded regions in (b) and (c) are the Voigt profiles which result from fitting the spectra; fit parameters can be found in SI Figure 5.

lifetime broadening of the states involved, which could lead to incorrect interpretations.[16] By fitting a sum of Voigt profiles to the CIE and CET cuts in Figures 3–5(b,c), we find the peak positions of the features as a function of incident energy and energy transfer. The peak positions are reported in Table 1. The energy splittings between subpeaks in a given feature, i.e., B2–B1, and subpeaks in different features, i.e., C1–B1, are also given in Table 1. The error in the positions of these features are 0.1 eV after accounting for the instrumental resolution and the error of the fits; the fitting is described in more detail in SI Figures 3–5. The fitting process struggled with low-intensity peaks that overlap with other features, i.e., the A2 feature in $[Ru^{III}(NH_3)_6]^{3+}$; as such their positions are noted as N/A in Table 1. In the following sections, the peak positions and the energy splittings between the various features are analyzed, allowing for information about the electronic structures of these three Ru-systems to be extracted.

2p3d RIXS Map of $[Ru^{III}(NH_3)_6]^{3+}$. The ground state valence electron configuration of the Ru^{III} complex $[Ru^{III}(NH_3)_6]^{3+}$ is 4d t_{2g}^5 e_g^0. Due to the vacancy in the t_{2g} orbitals, transitions into both the t_{2g} and e_g orbitals are possible (A and B features, Figure 1(a)). Looking first at the full $[Ru^{III}(NH_3)_6]^{3+}$ RIXS map in Figure 3(a), one can pick out 5 peaks: A1, A2, B0, B1, and B2. Out of these peaks, the A1 and B1 are the most distinct and lie on a diagonal of constant emission energy corresponding to the Lα_1 emission line ($3d_{5/2} \rightarrow 2p_{3/2}$, 2558 eV). Similarly, the A2 and B2 peaks lie on a diagonal of constant emission energy corresponding to the Lα_2 emission line ($3d_{3/2} \rightarrow 2p_{3/2}$, 2553.8 eV).

By fitting the CIE cuts shown in Figure 3(c), we find that the energy difference between the B1 and the B2 peaks is 4.3 eV and we interpret this to be primarily due to 3d spin–orbit coupling. We expect the A1 and A2 peaks be separated by the same amount, but it is difficult to establish the position of the A2 peak quantitatively due to its low intensity and because it overlaps with the B1 feature. This is particularly visible in Figure 3(a), in which the A2 peak manifests as an asymmetric broadening on the red edge of the B1 peak (~2837 eV). The

Table 1. Tabulated Positions of the Peaks Labeled in Figures 3–5 as Found by Fitting Cuts Taken along the Maxima of the Given Peak[a]

molecule	peak	position, eV $E_{inc.}(\Omega)$	position, eV $E_{trans.}(\Omega - \omega)$	splittings, eV Δ_{B-A} $E_{inc.}$ ($E_{trans.}$)	splittings, eV Δ_{C-B} $E_{inc.}$ ($E_{trans.}$)	splittings, eV Δ_{B2-B1}	splittings, eV Δ_{C2-C1}
	A1	2837.3	279.9				
	A2	N/A	N/A				
$[Ru^{III}(NH_3)_6]^{3+}$	B0	N/A	279.8	3.6 (3.2)		4.3	
	B1	2840.9	283.1				
	B2	2841.0	287.4				
	B1	2840.4	282.6				
$[Ru^{II}(bpy)_3]^{2+}$	B2	2840.3	286.6		3.9 (4.3)	4.0	
	C1	2844.3	286.9				
	B1	2841.5	283.9				
$[Ru^{II}(CN)_6]^{4-}$	B2	2841.5	288.0		1.8 (1.9)	4.1	4.1
	C1	2843.3	285.8				
	C2	2843.3	289.9				

[a]Peak positions that were difficult to distinguish with the fitting were marked as N/A. Energy splittings between peaks of interest are also included. Those outside of parentheses are splittings in the incident energy dimension and those within parentheses are splittings in the energy transfer dimension. After accounting for the instrumental resolution and fitting errors, the error in the position of the peaks is estimated to be ∼0.1 eV. The positions of the B1 peak in $[Ru^{III}(NH_3)_6]^{3+}$ were found by fitting this feature with one Voigt profile. See SI Figure 3 for additional details.

energy difference between the A1 and B1 peaks in the incident energy direction is 3.6 eV, as obtained from the fits of the CET cuts in Figure 3(b) and as reported in Table 1. This energy difference reports on the energy splitting between the t_{2g} and e_g orbitals and agrees well with previous measurements.[7,31] The energy difference between the A1 and the B1 features decreases to 3.2 eV in the energy transfer direction. The cause of the observed difference between $\Delta_{B\text{-}A}$ measured along the incident or the energy transfer is discussed in further detail in the discussion to follow.

Examining Figure 3(a) further, we see a low-intensity peak (B0) that cannot be explained as being due to the broadening of the A1 peak that lies along the same energy transfer. This peak can be more clearly seen in Figure 3(b). We tentatively assign this feature as being due to multiconfigurational mixing of 2p core excited states, i.e., $2p^5\ t_{2g}^6\ e_g^0$ and $2p^5\ t_{2g}^5\ e_g^1$, and is discussed in further detail later. Similar phenomena has been described in the context of 2p3d RIXS of 3d transition metals.[19]

Finally, Figure 3(c) shows that the B1 peak is asymmetric in the energy transfer axis. This asymmetry is due to a shoulder that is visible in the 2D map (Figure 3(a)) at high incident energies (2842 eV) and high energy transfers (284 eV). We hypothesize that this arises due to a deviation from octahedral symmetry caused by solute/solvent interactions and is also seen in the HERFD spectrum in Figure 2 as an asymmetric shoulder to the blue.

2p3d RIXS Map of $[Ru^{II}(bpy)_3]^{2+}$. The RIXS map of $[Ru^{II}(bpy)_3]^{2+}$, Figure 4(a), presents three 2D spectral features: B1, B2, and C1. The valence configuration of this Ru^{II} complex is 4d $t_{2g}^6\ e_g^0$ and can be used as a starting point when assigning these features. The absence of A features is expected as the t_{2g} orbitals are filled, and the B features are due to transitions from 2p orbitals into the empty e_g orbitals. The RIXS map of $[Ru^{II}(bpy)_3]^{2+}$ also possesses a C feature which arises due to the π^* orbitals of the bipyridine ligands having the appropriate symmetry to accept electron density from Ru 4d orbitals. This interaction yields transitions that involve orbitals with some metal-to-ligand charge transfer (MLCT) like character.

The CET and CIE cuts of the $[Ru^{II}(bpy)_3]^{2+}$ RIXS map are shown in Figure 4(b),(c), respectively. The 3d spin–orbit coupling constant of 4.0 eV, present in $[Ru^{II}(bpy)_3]^{2+}$, is encoded in the difference in position of the B1 and B2 peaks and obtained from fitting the CIE cut taken at the B1 peak's maximum value. CIE cuts at higher energies (∼2844 eV) present the interesting, yet weak, C_1 peak which corresponds to excitation into the Ru 4d-BPY π^* orbitals mentioned previously by Gawelda et al.[32] These metal–ligand π^* orbitals lie 3.9 eV above the e_g states, as reported by the energy difference, in the incident energy direction, between the B and C features, Δ_{C-B}. Previous theoretical studies and 2p4d RIXS measurements of $[Ru^{II}(bpy)_3]^{2+}$ have found that additional states with MLCT character which lie very close and at slightly lower energies than the 4d e_g orbitals.[33,24] Based on the above discussion, we attribute the asymmetric broadening of the B_1 peak (∼2841.5 eV) to Ru 2p → bpy π^* transitions, which are spectrally convoluted with the main B_1 peak.

2p3d RIXS Map of $[Ru^{II}(CN)_6]^{4-}$. The RIXS map of $[Ru^{II}(CN)_6]^{4-}$, Figure 5(a), contains two distinct features, B and C. These features consisting of the B1 and B2 peaks lie along a CIE of 2841.5 eV, while the C1 and C2 peaks lie along a CIE of 2843.5 eV, as shown in Figure 5(c). Similar to $[Ru^{II}(bpy)_3]^{2+}$, the B features correspond to initial transitions from 2p orbitals to 4d e_g orbitals and the C features correspond to transitions from Ru 2p orbitals to mixed Ru 4d-CN π^* orbitals with MLCT character. The splittings Δ_{B2-B1} and Δ_{C2-C1} are both found to be 4.1 eV (Table 1) and are due to 3d spin–orbit coupling, with emission from the $3d_{5/2}$ resulting in final states at lower energy transfers. The high intensity of the C features in $[Ru^{II}(CN)_6]^{4-}$ is due to the strong overlap between the Ru 4d orbitals and the CN ligands' π^* orbitals, which suggests that strong metal–ligand covalency is present in this complex. The energy difference, in the incident energy direction, between the B and C features is 1.8 eV and increases to 1.9 eV in the energy transfer direction.

DISCUSSION

Branching Ratio of the Lα Emissions. One point of interest concerning the subpeaks within a feature corresponding to $L\alpha_1$ and $L\alpha_2$ emissions, i.e., B1 and B2 peaks, is that

their intensity ratio is on the order of 10:1. While atomic theory calculations reproduce this ratio quite nicely, as reported in various X-ray emission data tables,[28,34] the reason for this ratio is not necessarily obvious. One could assume that the intensity ratio would be 3:2 given the degeneracies of the $3d_{5/2}$ and $3d_{3/2}$ orbitals, but as observed this is incorrect. The origin of this ≈10:1 intensity ratio is a total angular momentum sum rule discovered empirically in 1924 by Ornstein, Burger, and Dorgelo.[35] This sum rule was proven theoretically and presented in *The Theory of Atomic Spectra* by Condon and Shortley, where they state "...the sum of the strengths of the lines having a given initial level is proportional to the statistical weight $(2J + 1)$ of that initial level, and that the sum of the strengths of the lines having a given final level is proportional to the statistical weight of that final level."[36] This is represented pictorially for $L\alpha_1$ and $L\alpha_2$ transitions in SI Figure 1. This intensity ratio holds well for all of the spin–orbit split features in the three Ru complexes studied here. Though the calculations of Scofield[34,37] provide a more quantitative description of radiative decay rates, remembering this sum rule may provide a more intuitive understanding of the involved transitions, and help in identifying the spectral features in a Ru 2p3d RIXS map.

Insights into 3d → 4d Transitions from 2p3d RIXS. The 2p3d RIXS process is a second order process and in Ru includes two dipole allowed transitions: 2p → 4d and 3d → 2p. The energy transfer between the incident and emitted X-rays in this process corresponds to the energy splitting between the 3d and 4d orbitals. It should be noted that this covers the same energy range as the $M_{4,5}$ edges which correspond to excitations from the $3d_{5/2}$ orbitals and the $3d_{3/2}$ orbitals to the 4d orbitals, respectively. These transitions are formally forbidden for octahedral complexes when achieved through a one step, dipolar process, but the two step 2p3d RIXS process allows for 3d4d excited states to be seen, by virtue of coupling to intermediate states, with considerably higher intensity than would be observed in an $M_{4,5}$ experiment. The features seen in the CIE cuts given in Figures 3–5(a) then correspond to 3d4d excited states where the main features are primarily due to X-ray emission from the spin–orbit split $3d_{5/2}$ and $3d_{3/2}$ orbitals. These emissions are known as $L\alpha_1$ and $L\alpha_2$ for the $3d_{5/2}$ and $3d_{3/2}$, respectively. There may be additional features that appear along a CIE cut that arise due to 3d3d and 3d4d multiplet effects which further split the 3d or 4d orbitals. If 3d4d interactions are strong enough, then it may be that the 4d4d multiplet, 2p4d multiplet, 4d spin–orbit coupling, and 2p spin–orbit coupling also influence the peak shapes and identities.

As touched upon in the "Results" section, the splitting between two features, i.e., $\Delta_{B\text{-}A}$ in $[Ru^{III}(NH_3)_6]^{3+}$ and Δ_{C-B} in $[Ru^{II}(bpy)_3]^{2+}$, can be different in the incident energy and in the energy transfer dimensions. Since both directions assume initial state configurations of $2p^63d^{10}4d^N$, the differences in splittings likely arise due to effects present (or absent) when comparing the intermediate and final RIXS states: $2p^53d^{10}4d^{N+1}$, and $2p^63d^94d^{N+1}$, respectively.

For $[Ru^{III}(NH_3)_6]^{3+}$, the Δ_{B-A} value along the incident energy reports on the t_{2g}–e_g energy splitting in presence of a 2p hole, while along the energy transfer it reports on the energy splitting in presence of a 3d hole. Similarly, in $[Ru^{II}(bpy)_3]^{2+}$ and $[Ru^{II}(CN)_6]^{4-}$, the Δ_{C-B} value is the difference between the metal 4d and ligand π^* orbitals in the intermediate or final states, mainly due to changes in 3d4d interactions. Interestingly, differences in these Δ_{C-B} splittings between the two energy dimensions can report on the different strengths of metal–ligand interactions. As the energies of the 4d orbitals are altered between initial, intermediate, and final state electron configurations, the energies of the ligand π^* orbitals will also be altered with magnitudes determined by the strength of the metal–ligand π^* interactions. A molecular complex with strong metal 4d–ligand π^* interactions such as $[Ru^{II}(CN)_6]^{4-}$ will result in small differences (0.1 eV) between Δ_{C-B} in either dimension. Complexes with weaker 4d–ligand π^* interactions such as $[Ru^{II}(bpy)_3]^{2+}$ have larger differences (0.4 eV) between Δ_{C-B} in the incident energy and energy transfer directions.

The presence of the B0 peak in $[Ru^{III}(NH_3)_6]^{3+}$ is intriguing as it appears at an incident energy corresponding to a $2p_{3/2} \rightarrow$ 4d e_g transition (2841 eV), but appears at an energy transfer that would require a 3.6 eV higher emission energy than Ru $L\alpha_1$ (279.8 eV). As such, the nature of this feature is attributed to mixing between states with 4d valence configurations of $t_{2g}^5 e_g^1$ and $t_{2g}^6 e_g^0$ made possible by initial, intermediate, and final state effects that modulate the B0 peak intensity as seen in SI Figures 8 and 9. A similar mixing of core excited states has been seen in $L_{2,3}$ RIXS of Fe^{III} complexes, where the mixing of 3d valence configurations was made possible by the 2p spin–orbit coupling present in the RIXS intermediate states.[19]

CONCLUSION

The 2p3d RIXS measurement of solvated Ru complexes is shown to be a useful technique for investigating valence and core electronic structure of solution phase 4d transition metal complexes. The energy transfer between the two dipole transitions in this second order experiment allows for insights into 3d4d excited states that correspond to the normally dipole forbidden $M_{4,5}$ XAS transitions. The reduced lifetime broadening present in the energy transfer dimension allows for more quantitative assignments of spectral features and for more accurate comparisons with future calculations. The incident energy dimension of the RIXS maps provided insight into the valence electronic structure of the three complexes: t_{2g} orbitals of $[Ru^{III}(NH_3)_6]^{3+}$, e_g orbitals of $[Ru^{III}(NH_3)_6]^{3+}$, $[Ru^{II}(bpy)_3]^{2+}$, and $[Ru^{II}(CN)_6]^{4-}$, and 4d-ligand π^* orbitals of $[Ru^{II}(bpy)_3]^{2+}$ and $[Ru^{II}(CN)_6]^{4-}$. For all three of the complexes investigated, the energy transfer dimension of the RIXS maps exhibited features due to transitions involving the $3d_{5/2}$ and $3d_{3/2}$ orbitals which allowed for direct observation of the 3d spin–orbit coupling values: 4.3 eV for $[Ru^{III}(NH_3)_6]^{3+}$, 4.0 eV for $[Ru^{II}(bpy)_3]^{2+}$, and 4.1 eV for $[Ru^{II}(CN)_6]^{4-}$. These experimental SOC values will likely prove useful for theoretical methods when benchmarking their treatments of spin–orbit coupling. An additional feature, B0 appears in the $[Ru^{III}(NH_3)_6]^{3+}$ spectrum, which is likely a consequence of multiconfigurational mixing between closely lying electronic states in the ground or intermediate state manifolds. This suggests that calculations may need to include multireference methodology[38] to completely describe the electronic structure of these, and similar, transition metal complexes. The findings from this study present a framework for analyzing and understanding the 2p3d RIXS spectra for solvated 4d transition metal complexes, that are being actively studied with time-resolved X-ray spectroscopy at synchrotrons and X-ray free electron laser facilities.[30,32,39]

■ ASSOCIATED CONTENT

Supporting Information

The Supporting Information is available free of charge at https://pubs.acs.org/doi/10.1021/acs.inorgchem.3c00919.

Graphical representation of Lα branching ratio, incident energy vs emission energy RIXS maps, details of RIXS peak fitting, solid state RIXS maps with discussion comparing with solution phase RIXS, ligand field multiplet RIXS calculations of $[Ru^{III}(NH_3)_6]^{3+}$ (PDF)

All input .rcg and .rac files used in ligand field multiplet calculations of $[Ru^{III}(NH_3)_6]^{3+}$ (ZIP)

■ AUTHOR INFORMATION

Corresponding Authors

Munira Khalil − *Department of Chemistry, University of Washington, Seattle, Washington 98195, USA;* orcid.org/0000-0002-6508-4124; Email: mkhalil@uw.edu

Dimosthenis Sokaras − *SSRL, SLAC National Accelerator Laboratory, Menlo Park, California 94025, USA;* Email: dsokaras@slac.stanford.edu

Authors

Benjamin I. Poulter − *Department of Chemistry, University of Washington, Seattle, Washington 98195, USA;* orcid.org/0000-0002-2007-0319

Elisa Biasin − *Physical and Computational Sciences Directorate, Pacific Northwest National Laboratory, Richland, Washington 99352, United States*

Stanisław H. Nowak − *SSRL, SLAC National Accelerator Laboratory, Menlo Park, California 94025, USA*

Thomas Kroll − *SSRL, SLAC National Accelerator Laboratory, Menlo Park, California 94025, USA*

Roberto Alonso-Mori − *LCLS, SLAC National Accelerator Laboratory, Menlo Park, California 94025, USA;* orcid.org/0000-0002-5357-0934

Robert W. Schoenlein − *LCLS and Stanford PULSE Institute, SLAC National Accelerator Laboratory, Menlo Park, California 94025, USA*

Niranjan Govind − *Physical and Computational Sciences Directorate, Pacific Northwest National Laboratory, Richland, Washington 99352, United States;* orcid.org/0000-0003-3625-366X

Complete contact information is available at: https://pubs.acs.org/10.1021/acs.inorgchem.3c00919

Notes

The authors declare no competing financial interest.

■ ACKNOWLEDGMENTS

This work was supported by the U.S. Department of Energy, Office of Science, Office of Basic Energy Sciences, Division of Chemical Sciences, Geosciences, and Biosciences under Awards DE-SC0019277 and DE-SC0023249 (B.I.P. and M.K.), FWP 80818 (E.B. and N.G.), and Contracts DE-AC02-76SF00515 (E.B. and R.W.S.). B.I.P. acknowledges support by the NSF GRFP (No. DGE-1762114). This research benefited from computational resources provided by EMSL, a DOE Office of Science User Facility sponsored by the Office of Biological and Environmental Research and located at PNNL. PNNL is operated by Battelle Memorial Institute for the United States Department of Energy under DOE Contract No. DE-AC05-76RL1830. This research also used resources of the National Energy Research Scientific Computing Center (NERSC), a U.S. Department of Energy Office of Science User Facility operated under Contract No. DE-AC02-05CH11231. This research used resources of the Stanford Synchrotron Radiation Lightsource (SSRL) at SLAC National Accelerator Laboratory. SSRL is supported by the U.S. Department of Energy, Office of Science, Office of Basic Energy Sciences under Contract No. DE-AC02-76SF00515.

■ REFERENCES

(1) Kalyanasundaram, K. Photophysics, photochemistry and solar energy conversion with tris(bipyridyl)ruthenium(II) and its analogues. *Coord. Chem. Rev.* **1982**, *46*, 159−244.

(2) Tfouni, E.; Krieger, M.; McGarvey, B. R.; Franco, D. W. Structure, chemical and photochemical reactivity and biological activity of some ruthenium amine nitrosyl complexes. *Coord. Chem. Rev.* **2003**, *236*, 57−69.

(3) Naota, T.; Takaya, H.; Murahashi, S.-I. Ruthenium-Catalyzed Reactions for Organic Synthesis. *Chem. Rev.* **1998**, *98*, 2599−2660.

(4) Villani, E.; Sakanoue, K.; Einaga, Y.; Inagi, S.; Fiorani, A. Photophysics and electrochemistry of ruthenium complexes for electrogenerated chemiluminescence. *J. Electroanal. Chem.* **2022**, *921*, 116677.

(5) Gramage-Doria, R.; Bruneau, C. Ruthenium-catalyzed C−H bond functionalization in cascade and one-pot transformations. *Coord. Chem. Rev.* **2021**, *428*, 213602.

(6) Allardyce, C. S.; Dyson, P. J. Ruthenium in medicine: current clinical uses and future prospects. *Platinum Metals Rev.* **2001**, *45*, 62.

(7) Van Kuiken, B. E.; Valiev, M.; Daifuku, S. L.; Bannan, C.; Strader, M. L.; Cho, H.; Huse, N.; Schoenlein, R. W.; Govind, N.; Khalil, M. Simulating Ru L3-Edge X-ray Absorption Spectroscopy with Time-Dependent Density Functional Theory: Model Complexes and Electron Localization in Mixed-Valence Metal Dimers. *J. Phys. Chem. A* **2013**, *117*, 4444−4454.

(8) Damrauer, N. H.; Cerullo, G.; Yeh, A.; Boussie, T. R.; Shank, C. V.; McCusker, J. K. Femtosecond Dynamics of Excited-State Evolution in [Ru(bpy)3]2+. *Science* **1997**, *275*, 54−57.

(9) Qin, Y.; Peng, Q. Ruthenium Sensitizers and Their Applications in Dye-Sensitized Solar Cells. *International Journal of Photoenergy* **2012**, *2012*, 291579.

(10) Cordones, A. A.; Lee, J. H.; Hong, K.; Cho, H.; Garg, K.; Boggio-Pasqua, M.; Rack, J. J.; Huse, N.; Schoenlein, R. W.; Kim, T. K. Transient metal-centered states mediate isomerization of a photochromic ruthenium-sulfoxide complex. *Nat. Commun.* **2018**, *9*, 1989.

(11) Baker, M. L.; Mara, M. W.; Yan, J. J.; Hodgson, K. O.; Hedman, B.; Solomon, E. I. K- and L-edge X-ray absorption spectroscopy (XAS) and resonant inelastic X-ray scattering (RIXS) determination of differential orbital covalency (DOC) of transition metal sites. *Coord. Chem. Rev.* **2017**, *345*, 182−208.

(12) de Groot, F.; Kotani, A. *Core Level Spectroscopy of Solids*; CRC Press, 2008; p 111−115.

(13) Alperovich, I.; Smolentsev, G.; Moonshiram, D.; Jurss, J. W.; Concepcion, J. J.; Meyer, T. J.; Soldatov, A.; Pushkar, Y. Understanding the Electronic Structure of 4d Metal Complexes: From Molecular Spinors to L-Edge Spectra of a di-Ru Catalyst. *J. Am. Chem. Soc.* **2011**, *133*, 15786−15794.

(14) Getty, K.; Delgado-Jaime, M. U.; Kennepohl, P. Assignment of Pre-edge Features in the Ru K-edge X-ray Absorption Spectra of Organometallic Ruthenium Complexes. *Inorganica chimica acta* **2008**, *361*, 1059−1059.

(15) Levin, N.; Peredkov, S.; Weyhermüller, T.; Rüdiger, O.; Pereira, N. B.; Grötzsch, D.; Kalinko, A.; DeBeer, S. Ruthenium 4d-to-2p X-ray Emission Spectroscopy: A Simultaneous Probe of the Metal and the Bound Ligands. *Inorg. Chem.* **2020**, *59*, 8272−8283.

(16) Glatzel, P.; Bergmann, U. High resolution 1s core hole X-ray spectroscopy in 3d transition metal complexes - Electronic and structural information. *Coord. Chem. Rev.* **2005**, *249*, 65−95.

(17) Sreekantan Nair Lalithambika, S.; Golnak, R.; Winter, B.; Atak, K. Electronic Structure of Aqueous [Co(bpy)3]2+/3+ Electron Mediators. *Inorg. Chem.* **2019**, *58*, 4731−4740.
(18) Jay, R. M.; Eckert, S.; Fondell, M.; Miedema, P. S.; Norell, J.; Pietzsch, A.; Quevedo, W.; Niskanen, J.; Kunnus, K.; Föhlisch, A. The nature of frontier orbitals under systematic ligand exchange in (pseudo-)octahedral Fe(ii) complexes. *Phys. Chem. Chem. Phys.* **2018**, *20*, 27745−27751.
(19) Kunnus, K.; Zhang, W.; Delcey, M. G.; Pinjari, R. V.; Miedema, P. S.; Schreck, S.; Quevedo, W.; Schröder, H.; Föhlisch, A.; Gaffney, K. J.; Lundberg, M.; Odelius, M.; Wernet, P. Viewing the Valence Electronic Structure of Ferric and Ferrous Hexacyanide in Solution from the Fe and Cyanide Perspectives. *J. Phys. Chem. B* **2016**, *120*, 7182−7194.
(20) Norell, J.; Jay, R. M.; Hantschmann, M.; Eckert, S.; Guo, M.; Gaffney, K. J.; Wernet, P.; Lundberg, M.; Föhlisch, A.; Odelius, M. Fingerprints of electronic, spin and structural dynamics from resonant inelastic soft X-ray scattering in transient photo-chemical species. *Phys. Chem. Chem. Phys.* **2018**, *20*, 7243−7253.
(21) Wernet, P.; et al. Orbital-specific mapping of the ligand exchange dynamics of Fe(CO)5 in solution. *Nature* **2015**, *520*, 78−81.
(22) Thomas, R.; Kas, J.; Glatzel, P.; Al Samarai, M.; de Groot, F. M. F.; Alonso Mori, R.; Kavčič, M.; Zitnik, M.; Bucar, K.; Rehr, J. J.; Tromp, M. Resonant Inelastic X-ray Scattering of Molybdenum Oxides and Sulfides. *J. Phys. Chem. C* **2015**, *119*, 2419−2426.
(23) Takahashi, H.; Suzuki, H.; Bertinshaw, J.; Bette, S.; Mühle, C.; Nuss, J.; Dinnebier, R.; Yaresko, A.; Khaliullin, G.; Gretarsson, H.; Takayama, T.; Takagi, H.; Keimer, B. Nonmagnetic $J = 0$ State and Spin-Orbit Excitations in K_2RuCl_6. *Phys. Rev. Lett.* **2021**, *127*, 227201.
(24) Biasin, E.; Nascimento, D. R.; Poulter, B. I.; Abraham, B.; Kunnus, K.; Garcia-Esparza, A. T.; Nowak, S. H.; Kroll, T.; Schoenlein, R. W.; Alonso-Mori, R.; Khalil, M.; Govind, N.; Sokaras, D. Revealing the bonding of solvated Ru complexes with valence-to-core resonant inelastic X-ray scattering. *Chem. Sci.* **2021**, *12*, 3713−3725.
(25) Nascimento, D. R.; Biasin, E.; Poulter, B. I.; Khalil, M.; Sokaras, D.; Govind, N. Resonant inelastic x-ray scattering calculations of transition metal complexes within a simplified time-dependent density functional theory framework. *J. Chem. Theory Comput.* **2021**, *17*, 3031−3038.
(26) Berger, G.; Wach, A.; Sá, J.; Szlachetko, J. Reduction Mechanisms of Anticancer Osmium(VI) Complexes Revealed by Atomic Telemetry and Theoretical Calculations. *Inorg. Chem.* **2021**, *60*, 6663−6671.
(27) Kim, Y.-J.; Clancy, J. P.; Gretarsson, H.; Cao, G.; Singh, Y.; Kim, J.; Upton, M. H.; Casa, D.; Gog, T. Probing electronic excitations in iridates with resonant inelastic X-ray scattering and emission spectroscopy techniques. *arXiv (Strongly Correlated Electrons)*, 9 May 2018, 1805.03612, ver. 1. DOI: 10.48550/arXiv.1805.03612.
(28) Keski-Rahkonen, O.; Krause, M. O. Total and partial atomic-level widths. *At. Data Nucl. Data Tables* **1974**, *14*, 139−146.
(29) Nowak, S. H.; Armenta, R.; Schwartz, C. P.; Gallo, A.; Abraham, B.; Garcia-Esparza, A. T.; Biasin, E.; Prado, A.; Maciel, A.; Zhang, D.; et al. A versatile Johansson-type tender x-ray emission spectrometer. *Rev. Sci. Instrum.* **2020**, *91*, 033101.
(30) Van Kuiken, B. E.; Huse, N.; Cho, H.; Strader, M. L.; Lynch, M. S.; Schoenlein, R. W.; Khalil, M. Probing the electronic structure of a photoexcited solar cell dye with transient X-ray absorption spectroscopy. *J. Phys. Chem. Lett.* **2012**, *3*, 1695−1700.
(31) Sham, T. K. X-ray absorption spectra of ruthenium L edges in hexaammineruthenium trichloride. *J. Am. Chem. Soc.* **1983**, *105*, 2269−2273.
(32) Gawelda, W.; Johnson, M.; De Groot, R.; Abela; Bressler, C.; Chergui, M. Electronic and molecular structure of photoexcited [RuII(bpy) 3]2+ probed by picosecond X-ray absorption spectroscopy. *J. Am. Chem. Soc.* **2006**, *128*, 5001−5009.
(33) Wilson, G. J.; Will, G. D. Density-functional analysis of the electronic structure of tris-bipyridyl Ru(II) sensitisers. *Inorg. Chim. Acta* **2010**, *363*, 1627−1638.
(34) Scofield, J. H. Relativistic hartree-slater values for K and L X-ray emission rates. *Atomic Data and Nuclear Data Tables* **1974**, *14*, 121−137.
(35) Ornstein, L. S.; Burger, H. C. Strahlungsgesetz und Intensität von Mehrfachlinien. *Zeitschrift für Physik* **1924**, *24*, 41−47.
(36) Condon, E. U.; Shortley, G. H. *The Theory of Atomic Spectra*; Cambridge University Press, 1935.
(37) Scofield, J. H. Radiative Decay Rates of Vacancies in the *K* and *L* Shells. *Phys. Rev.* **1969**, *179*, 9−16.
(38) Josefsson, I.; Kunnus, K.; Schreck, S.; Föhlisch, A.; de Groot, F.; Wernet, P.; Odelius, M. Ab Initio Calculations of X-ray Spectra: Atomic Multiplet and Molecular Orbital Effects in a Multiconfigurational SCF Approach to the L-Edge Spectra of Transition Metal Complexes. *J. Phys. Chem. Lett.* **2012**, *3*, 3565−3570.
(39) Kim, Y.; Ma, R.; Lee, J.; Harich, J.; Nam, D.; Kim, S.; Kim, M.; Ochmann, M.; Eom, I.; Huse, N.; Lee, J. H.; Kim, T. K. Ligand-Field Effects in a Ruthenium(II) Polypyridyl Complex Probed by Femtosecond X-ray Absorption Spectroscopy. *J. Phys. Chem. Lett.* **2021**, *12*, 12165−12172.